




# A framework for printing, detection, tracking, and registration of deformable grids

Tyler S. Kenyon<sup>a</sup> , Allan D. Spence<sup>a</sup>  and David W. Capson<sup>b</sup> 

<sup>a</sup>McMaster University, Canada; <sup>b</sup>University of Victoria, Canada

## ABSTRACT

This paper proposes a novel framework for high resolution printing, detection, tracking, and registration of deformable grids. The undeformed dot feature grid is created on the target surface using a flat bed inkjet printer. After deformation, the surface is imaged using close-range monocular vision, and the dots are detected and localized to sub-pixel accuracy. A novel, deformation invariant grid registration topological map and associated algorithms are used to track features between subsequent video frames. By matching the map to the undeformed grid geometry, stretching or compression of the distance between the dots can be used to compute the material strains. Accuracy, repeatability, and computation time for several image based dot feature detectors are compared, and experimental laboratory results demonstrate consistent robustness of the method under practical imaging conditions.

## KEYWORDS

Machine vision; blob feature detection; dot grid printing and tracking

## 1. Introduction

Deforming flat sheets into final product shapes is a frequent manufacturing process. Examples range from refrigerator inside liners to metal automobile bodies. Simple vacuum forming is accomplished by warming the thermoplastic sheet and then using suction to force the material against a mold of the desired shape. Sheet metal forming depends on high force presses. In either case, there is a desire to save cost and mass by minimizing material thickness, so long as excessive thinning or wrinkling are avoided. Prediction [5] can reduce design and process iteration, but, particularly for new materials, characteristic property determination and experimental validation remain essential.

A standardized method is the Limiting Dome Height test [7] that can be used to plot safe, marginal, and failure strain regions on a material Forming Limit Diagram (Fig. 1). When both the major  $\varepsilon_1$  and minor  $\varepsilon_2$  principal surface strains are positive (tension), the material will stretch until it cracks. When the minor strain is negative (compression), deformation can continue until wrinkles appear.

Strain is measured by determining, to a high resolution, the change in distances between specific surface locations before and after forming. To accomplish this, we first print a regular grid onto the undeformed sheet.

After forming, close-range computer vision is used to detect the deformed grid elements, track them from frame to frame, and maintain an invariant registration with the original grid.

The remainder of this paper is organized as follows. Grid printing is described in Section 2. Section 3 evaluates several image-based feature detectors using both real and synthetic datasets. Section 4 describes a new technique for inter-frame grid tracking, and Section 5 introduces a novel algorithm for deformation-invariant grid registration. The paper concludes in Section 6.

## 2. Grid printing

### 2.1. Strain measurement grids

Undeformed strain measurement grids are typically modest resolution random speckle patterns [6][24], circles [2], squares, or dots. For squares, the corners can be considered as vertices [13]. Dot centers can alternatively be used. After forming, the surface strains can be computed as described in [23]. Three vertices from a single grid element establish a local (undeformed) triangle  $AOB$  (Fig. 2). After forming, the distorted vertices define the triangle  $A'OB'$ . The relative displacement of

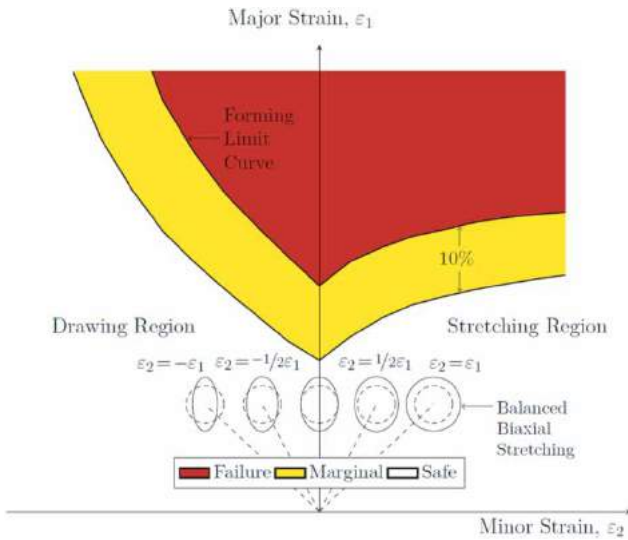


**Figure 1.** A typical forming limit diagram [10].

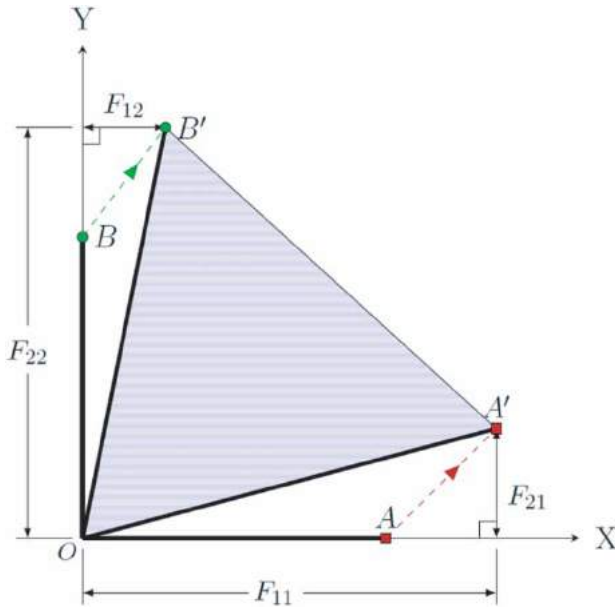


**Figure 2.** Homogenous deformation of a triangular grid element.

the initial grid vertex coordinates,  $(X_A, Y_A)$  and  $(X_B, Y_B)$ , to the deformed coordinates,  $(x_{A'}, y_{A'})$  and  $(x_{B'}, y_{B'})$ , are expressed by the linear system:

$$\begin{bmatrix} x_{A'} \\ y_{A'} \end{bmatrix} = \begin{bmatrix} F_{11} & F_{12} \\ F_{21} & F_{22} \end{bmatrix} \begin{bmatrix} X_A \\ Y_A \end{bmatrix}, \quad (2.1)$$

$$\begin{bmatrix} x_{B'} \\ y_{B'} \end{bmatrix} = \begin{bmatrix} F_{11} & F_{12} \\ F_{21} & F_{22} \end{bmatrix} \begin{bmatrix} X_B \\ Y_B \end{bmatrix}$$

where  $F_{2 \times 2}$  represents a constant second order deformation gradient tensor. After rearranging and solving

for  $F$ :

$$\begin{bmatrix} F_{11} \\ F_{12} \\ F_{21} \\ F_{22} \end{bmatrix} = D \begin{bmatrix} Y_B & -Y_A & 0 & 0 \\ -X_B & X_A & 0 & 0 \\ 0 & 0 & Y_B & -Y_A \\ 0 & 0 & -X_B & X_A \end{bmatrix} \begin{bmatrix} x_{A'} \\ x_{B'} \\ y_{A'} \\ y_{B'} \end{bmatrix} \quad (2.2)$$

where  $D = 1/(X_A Y_B - X_B Y_A)$ . The eigenvalues,  $\lambda_{1,2}$ , of  $F$  can be computed using Singular Value Decomposition, and the relationship:  $\varepsilon_{1,2} = \ln(\lambda_{1,2})$  defines the surface strains.

For constant strains, a circle grid element will deform into an ellipse, and measurement can be performed by using computer vision to determine the ellipse major and minor axes [4]. A strain gradient across the ellipse cannot be measured, and it is impractical to print the circles much smaller than the standard 2.54 mm diameter. Similarly, square grids cannot in practice be printed smaller than this pitch. Ink cracking at higher strains is also a concern. A regular grid of small diameter dots that, over unlimited areas, can be printed and detected to a higher resolution than the commercial GOM Argus [8] or ViALUX AutoGrid [25] systems, was therefore chosen for this work.

## 2.2. Large area high resolution printing

Although electrochemical etching methods can be used on steel sheets to create the grid, resolution is not adequate, and area is limited to the size of the stencil. Screen printing is usually chosen for aluminum and plastic, but again resolution and maximum area are limited. Therefore, a high resolution programmable solution was employed. First, a regular grid pattern with 0.7 mm diameter solid dots, on a 1 mm pitch, was designed in AutoCAD® [1]. Actual printing was performed using a 1440 × 1440 dots per inch resolution Roland LEJ-640 1625 mm wide flatbed inkjet printer [22]. (Fig. 3) A valuable characteristic is that the ultraviolet light curable ink can stretch up to 220 percent, and hence is unlikely to crack under the expected strains. Omitted dots (as can be observed in Fig. 3(b)) are used for inter-frame video fiducial tracking, as described in Section 4.

## 3. Grid-feature detection

### 3.1. Blob detection

To robustly detect and accurately localize each dot-grid feature, we adapted an existing solution from the literature, and thereby leveraged the extensive body of work regarding feature detection. Several image-based feature detection algorithms were investigated and four blob

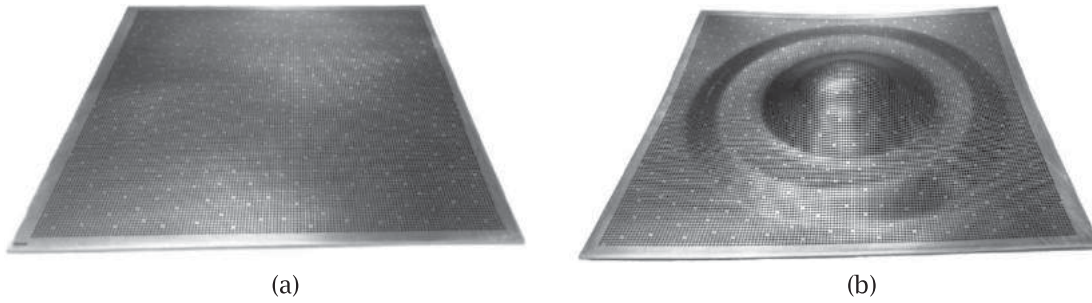


**Figure 3.** Example of inkjet dot grid printing. (a) Inkjet dot grid printed onto flat AA5754-O aluminum sheet; (b) Dot grid after forming.

detectors were identified for further investigation. The four candidate detectors are described briefly below.

The Maximally Stable Extremal Regions (MSER) blob detector was developed by Matas et al. [18]. MSERs are an affine-invariant stable subset of the connected components in a thresholded image. All possible threshold values are tested and the *maximally stable extremal regions* are those that exhibit the smallest change over a range of different thresholds.

The Scale Invariant Feature Transform (SIFT) is a detector and descriptor developed by Lowe [16, 17], who pioneered the Difference of Gaussians approach. To simplify computation, the DoG operator,  $D(x, y, \sigma)$ , approximates the scale-normalized Laplacian of Gaussian [15] by computing the difference of two adjacent scale-space images:

$$D(x, y, \sigma) = L(x, y, k\sigma) - L(x, y, \sigma) \quad (3.1)$$

where  $L(x, y, \sigma)$  denotes the input image after convolution with a variable-scale Gaussian kernel and  $k$  is a constant multiplicative factor representing the difference between two nearby scales.

Speeded-Up Robust Features (SURF) is a local invariant feature detector and descriptor developed by Bay et al. [3]. Fundamentally, the SURF algorithm uses an approximation of the determinant of the Hessian matrix:

$$\det \mathcal{H}_{approx} = D_{xx}D_{yy} + (wD_{xy})^2 \quad (3.2)$$

where  $D_{xx}$ ,  $D_{yy}$ , and  $D_{xy}$  denote box convolution filters that approximate the second order Gaussian derivatives and  $w$  is an experimentally determined balancing weight. To enable fast computation of the box convolution filters, integral images [26] are used. False positives are eliminated using non-maximum suppression [19] in a  $3 \times 3 \times 3$  neighborhood, and the feature is localized to sub-pixel resolution.

The Center Surround Extrema (CenSurE) detector is based on a bi-level Laplacian of Gaussian filter. Although a circular filter provides rotational invariance, CenSurE uses a hexagonal or octagonal filter to reduce runtime.

These filters can be computed very quickly using slanted integral images so that the computation time required for each filter is independent of its size. CenSurE computes a filter response at every pixel and uses non-maximum suppression to eliminate the false positive errors. A scale-adapted Harris measure [9] is used to suppress the response from edges. A popular implementation of the CenSurE detector – named “STAR” – uses a filter with a shape resembling the Star of Lakshmi.

### 3.2. Detector evaluation

#### 3.2.1. Synthetic dataset

To evaluate the four blob detectors selected from the literature, a synthetic image sequence was generated using ray-tracing software. With the exact location of each feature derived from the projective geometry of the synthetically-generated image, the ray-traced images could provide ground truth data which was used to measure the accuracy and precision of the feature detection process. In total, a sequence of 15 progressive frames was rendered using the Persistence of Vision Ray-tracer [21], with each image depicting a flat sheet of aluminum marked with a dot-grid pattern. The virtual camera was rotated throughout the sequence so that, with each successive frame, the angle of incidence grew increasingly oblique. This corresponded with greater depth-of-field blur in each image as the sequence progressed. To ensure photo-realism: lighting, aperture, focal length, and the material properties of the aluminum sheet were all fine-tuned to match real images captured using a camera.

#### 3.2.2. Benchmarking criteria

To meet the requirements of our application, a feature detector must satisfy the following four criteria:

1. Coverage: For optimal results, all grid features within the field of view of the image should be detected. In practice, some undetected grid features near the image borders are acceptable. However spurious grid features (i.e., false positive errors) and undetected

grid features (i.e., false negative errors) must be minimized to enable subsequent processing stages.

2. Accuracy: Like any metrological application, strain analysis demands a high degree of accuracy. For sufficiently low strain uncertainty, sub-pixel accuracy is required.
3. Repeatability: Individual grid features must be reliably detected across multiple images in the sequence, despite changes to scale, rotation, and illumination.
4. Computation Time: For practical use within an industrial environment, computation time should approach the camera data acquisition rate.

### 3.2.3. Test platform

For this experiment, existing implementations of the MSER, SIFT, STAR, and SURF detectors were obtained from OpenCV 2.4.6. Each detector's response was filtered such that only dark blobs were recorded. The detection and evaluation software were compiled with GCC 4.6.3 using -O2 optimization. The evaluation was performed on a 2.8 GHz Intel Core i7 running Ubuntu 12.04 LTS. Eight-bit grayscale images with a resolution of 1024 × 768 pixels were used.

### 3.2.4. Experimental results

**3.2.4.1. Coverage and repeatability.** The MSER detector demonstrated relatively poor coverage and repeatability. On average, 7% of all available features went undetected throughout the image sequence, and false positive errors were prominent. These errors appeared scattered throughout the image without a discernible pattern. The rate of recurrence and location of these errors would inhibit robust grid tracking.

The SIFT detector exhibited the worst coverage and repeatability of any detector evaluated herein. As the sequence progressed, the number of false positive errors increased dramatically, often appearing in streaks that stretched across the image. At its best, the SIFT algorithm detected 87.4% of available features. By the end of the sequence, only 62.2% of features were detected. On average, SIFT would re-detect only 79.6% of the features previously discovered from the preceding frame.

Except for a few false negative errors appearing throughout the image sequence, the STAR detector demonstrated near perfect coverage and repeatability. For every frame in the sequence, over 99% of all available features were detected. Re-detection was accordingly strong, with an average rate of 97.1%.

The SURF detector achieved near flawless coverage. For a typical frame, 99.4% of all available features were detected. Although a few false negative errors did occur, these undetected grid features only appeared at the very edge of the frame where their effect is negligible. No

false positive errors were reported. The detection and re-detection statistics for Frame 7 are summarized in Tab. 1.

**Table 1.** Number of features detected as a percentage of total features present (taken from Frame 7 of the image sequence). Re-detection measures the ability of each detector to detect the same feature in both the current frame and the preceding frame.

Detector	Features Detected (%)	Features Re-detected (%)
MSER	94.5	87.8
SIFT	83.7	81.2
STAR	99.7	97.2
SURF	99.4	96.8

**Table 2.** Localization Error as measured using a typical frame (7 of 15) from the image sequence.

Detector	Mean ± Std. Dev. (pixels)	Error > 1 pixel (%)	Error > 5 pixels (%)
MSER	0.01 ± 0.26	1.50	0.33
SIFT	0.39 ± 0.08	0.20	0.01
STAR	0.03 ± 0.48	1.24	0.47
SURF	0.02 ± 0.09	0.00	0.00

**3.2.4.2. Accuracy.** The MSER features were detected with relatively poor accuracy and precision (see Fig. 4(a)). The average localization error was 0.01 pixels, with a standard deviation of 0.26 pixels. Most of the extreme localization errors occurred at the image borders where only a fraction of each feature is within the field of view.

The results from the SIFT detector were biased by a systematic error introduced during the detection process. The mean localization error was 0.39 pixels (X-error: +0.27 pixels, Y-error: +0.28 pixels). However, SIFT demonstrated the best precision of any detector evaluated herein, with a standard deviation of 0.08 pixels. The bias can be seen throughout the error distribution in Fig. 4(b).

The STAR detector produced the worst precision of any detector evaluated herein (see Fig. 4(c)). Due to the fact that STAR does not use sub-pixel interpolation, the standard deviation of the feature localization error was 0.48 pixels. 1.24% of the STAR features were detected with an error greater than 1 pixel, and 0.47% of features were detected with an error greater than 5 pixels. Despite poor precision, the mean localization error was only 0.03 pixels.

SURF features were detected with the best accuracy and precision (Fig. 4(d)). The mean localization error was only 0.02 pixels, and the maximum error produced during the detection process was limited to 0.36 pixels. The standard deviation across all images in the sequence was 0.09 pixels.

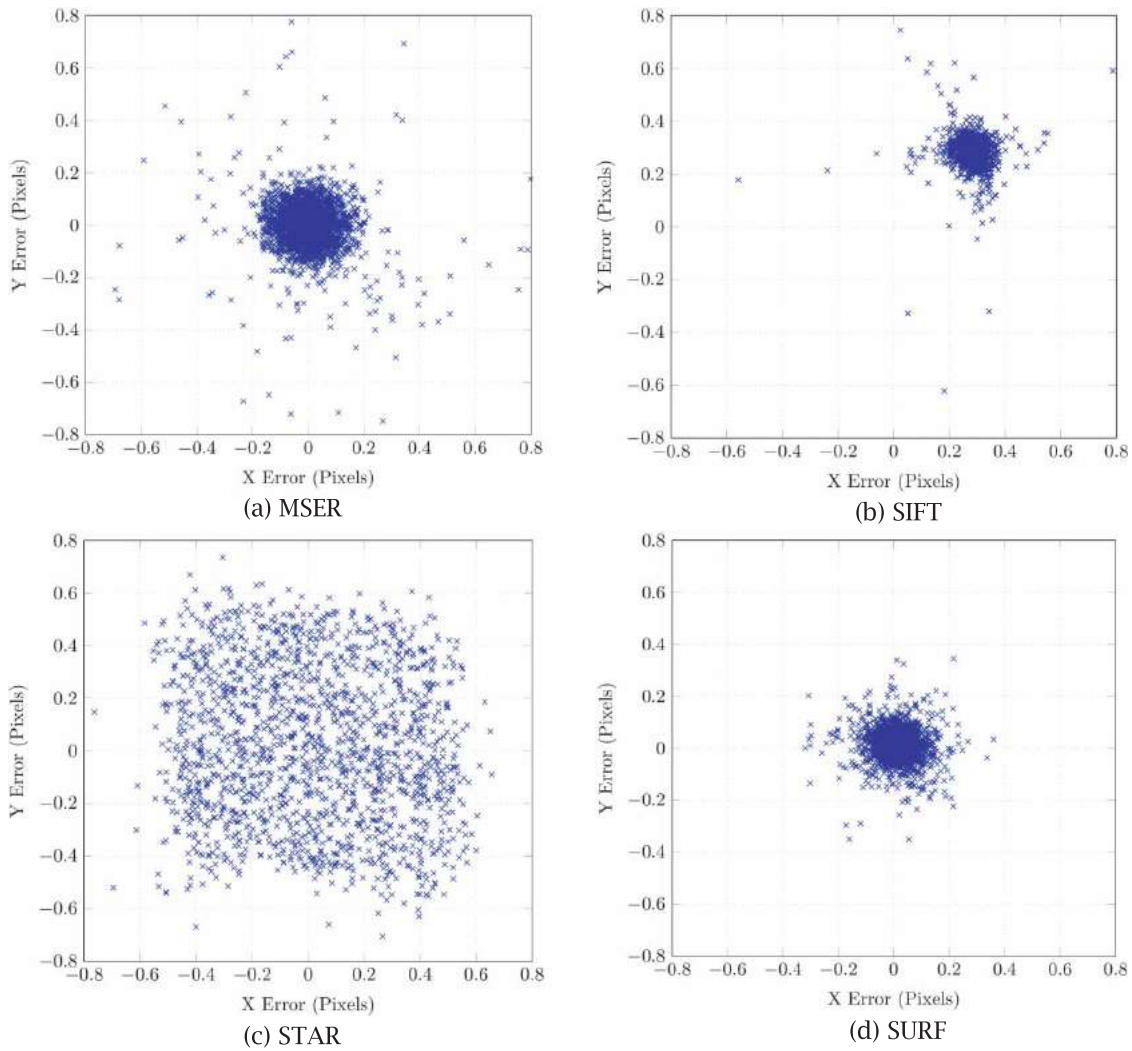


**Figure 4.** Error distribution of detected features relative to ground truth values.

**3.2.4.3. Computational performance.** The computational performance of each detector was evaluated by measuring the time required to detect all features within a frame. For our sample sizes, for  $n$  features, all four detectors performed in linear  $O(n)$  time, with varying growth constants for each detector. The STAR detector demonstrated the best runtime, followed by the MSER, SURF, and SIFT detectors, respectively. The computational performance of each detector is detailed in Tab. 3.

**Table 3.** Computation time for a typical frame with approximately 900 features detected.

Detector	Runtime (ms)	Frames Per Second
MSER	116.90	8.55
SIFT	482.36	2.07
STAR	38.50	25.98
SURF	199.79	5.01

### 3.3. Grid-feature localization on formed aluminum

#### 3.3.1. Methodology

To validate the results of the synthetic dataset analysis, and determine the applicability of this research to practical (industrial) imaging conditions, the feature detection algorithms were also applied to real images of a formed aluminum dome.

After applying the grid pattern, the aluminum sheets were formed into a punched dome by a laboratory stamping press. The stamped sheets were then imaged using a Point-Grey Dragonfly camera. 8-bit grayscale images were captured at 1.5 frames per second with a resolution of  $1024 \times 768$  pixels. A 12 mm low-distortion Cosmicar-Pentax fixed-focus lens was used with a 1 mm extension ring to facilitate close-range imaging ( $\sim 5$  cm object-to-sensor distance). The camera was mounted as the end-effector of a portable articulated-arm coordinate measuring machine. To avoid the need for robotic path programming, the camera was hand-guided

by scanning the target surface in a sweeping motion (Fig. 5).



**Figure 5.** A hand-guided camera mounted on an articulated arm coordinate measuring machine (from [13], used with permission).

### 3.3.2. Experimental results

Similar to the synthetic dataset results, the MSER algorithm performed poorly when operating on real video of formed aluminum. The number of false positive errors was unacceptably high, and many instances of poor accuracy occurred near the image borders. The MSER detector was relatively unaffected by the heavy depth-of-field blur caused by the curvature of the formed dome.

SIFT also exhibited similar results. As with the synthetic dataset, large streaks of undetected dot features appear throughout each image. SIFT had slightly improved coverage using the real dataset, but false positive errors occurred at a similar frequency.

The STAR detector produced almost identical results using the real and synthetic datasets. In both instances, only a few grid features went undetected in each image. False positive errors did not occur, except one or two cases where surface defects had split a dot-feature into two parts. STAR operated with poor accuracy near the detection borders.

In excellent agreement with the synthetic results, the SURF detector performed extremely well using the real dataset. Despite heavy depth-of-field blur, few features remained undetected, and those omissions only occurred, harmlessly, near the image borders. Except for those caused by rare (one or two) unnatural surface imperfections (such as deep scratches), there were no false positive errors.

### 3.4. Discussion

Overall, the results from the synthetic and real datasets were in excellent agreement. These experiments demonstrate decisively that the SURF algorithm is the most accurate and robust of all detectors evaluated herein. Even under adverse imaging conditions including specular reflection and heavy depth-of-field blur, the SURF detector exceeded our requirements. SURF features were localized with a mean error less than  $1/40$  pixels and a standard deviation less than  $1/10$  pixels. Except for a few (negligible) undetected features near the image border, SURF demonstrated flawless coverage and repeatability. Furthermore, the computational performance of the SURF algorithm was deemed sufficient; for a typical frame with about 900 features detected, SURF processed just over 5 frames per second. This rate could easily be increased by using inexpensive parallel computing hardware such as the Intel Xeon Phi [11] or any CUDA-enabled NVIDIA GPU [20].

Converting to actual length units and strain percentage, on average there are approximately 40 pixels per mm. The maximum error for SURF is 0.36 pixels or 0.009 mm. For a printed grid with a 1 mm pitch, this is below one percent.

## 4. Inter-frame grid tracking

Matching the features from one image with the corresponding features in a second image has traditionally been accomplished using feature description. Feature descriptors encode details about the local neighborhood of a feature, especially information that is invariant to photometric and geometric fluctuations. However, the difference between the appearances of each dot feature is too subtle to be distinguished using a feature vector. Consequently, new approaches to feature tracking and matching were required.

In [14], we proposed a novel technique for motion tracking of gridded surfaces using topological structure. Therein, hand-drawn fiducials were placed between the lines of a square grid, and tracked by comparing active pixel ratios within thresholded connected components. The topological approach was chosen to reduce the dimensionality of the inter-frame transformation from a generic homography (eight continuous degrees of freedom) to discrete shifts in the directions of the grid axes. This reduction permitted the optimization to use an exhaustive search to test all likely grid shifts. Herein, we describe a similar technique that has been adapted to use a dot-grid pattern with negative fiducial tracking.

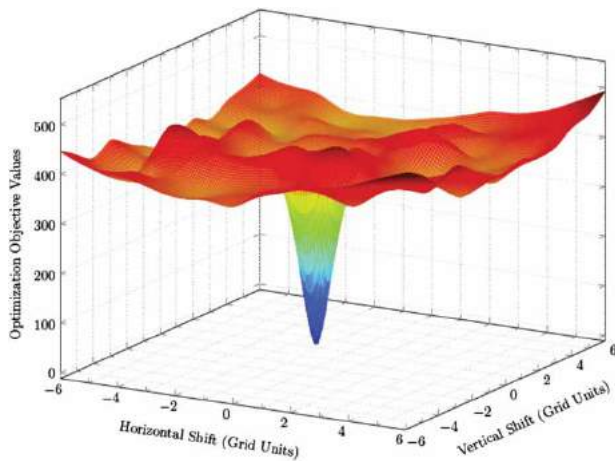


**Figure 6.** Objective function output for typical inter-frame motion [14]. A large downward spike indicating the minimum objective value represents the best estimate for inter-frame grid registration.

#### 4.1. Extracting topological structure

To extract the topological structure of the grid, dot-features are first localized with sub-pixel accuracy using the SURF detector (Fig. 7(a)). The centroid of each feature is then used to compute a Delaunay triangulation (Fig. 7(b)). Since the nearest neighbor graph is a sub-graph of the Delaunay triangulation, this approach allows neighboring features to be easily discovered using a breadth first search. The resulting structure is filtered geometrically and topologically so that only a regularly-ordered, 4-neighbor topology remains.

#### 4.2. Inter-frame registration

As described in section 3.1, some dot-features were irregularly omitted from the grid pattern in order to facilitate

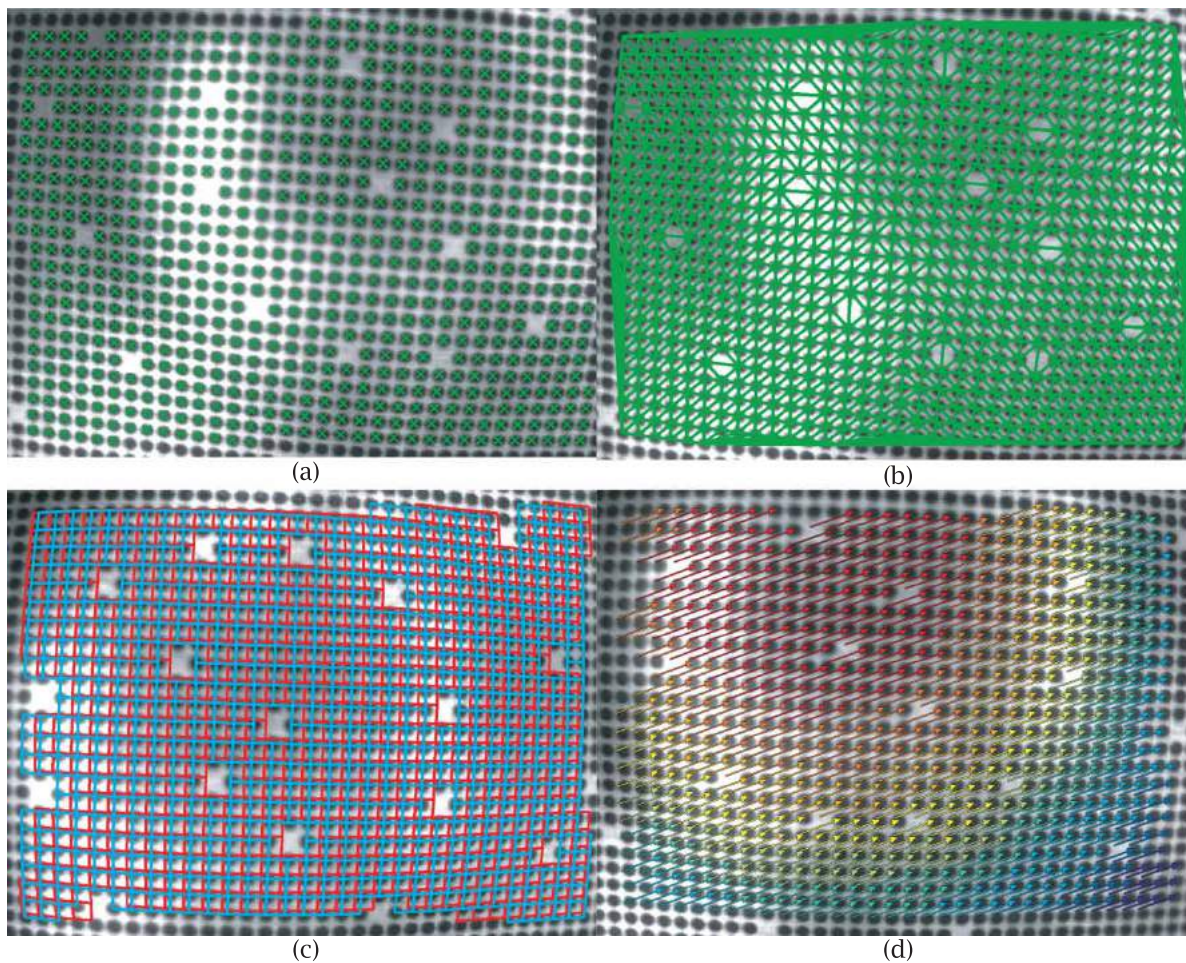


**Figure 7.** (a) Sub-pixel dot-feature detection using the SURF algorithm. (b) Delaunay triangulation of the detected dot-features. (c) An optimization objective function measures aggregate grid similarity between adjacent frames: (red) previous frame; (cyan) current frame. (d) Grid-feature tracking between frames. Color indicates the magnitude of each vector. Note the parallax effect from the curvature of the dome.

negative fiducial tracking. This approach eliminates the need to explicitly detect and describe fiducial features. After extracting the topological structure of the dot-grid pattern, the approximate locations of each missing dot are inferred, and then incorporated as salient nodes in the topology. Regular nodes are assigned a common metric value ( $\sigma = 1$ ), while salient nodes are given an extreme metric value ( $\sigma = 100$ ). The metric values are collected for each frame and used to measure aggregate grid similarity between adjacent frames (Fig. 7(c)). To this end, the topological representations of each frame are aligned so that rotation is eliminated as a possible degree of freedom in the optimization. The current and previous frames are then logically overlaid and an optimization objective function (Eq. 4.1) tests all possible grid shifts:

$$F(i, j) = \sum_{\substack{(x,y)|(x,y) \in G^k \\ (x+i,y+j) \in G^{k-1}}} (\sigma_{x,y}^k - \sigma_{x+i,y+j}^{k-1})^2 + P(i, j) \quad (4.1)$$

where  $i, j$  define the inter-frame shift, and variables  $x, y$  denote the location of the node in the  $k$ th topological representation of the grid,  $G^k$ . The penalty term,  $P(i, j) = \sqrt{i^2 + j^2}$ , represents the Euclidean distance of the grid shift.

At every overlaid node where both frames have a metric defined, the sum of square differences is computed. This sum is generated across all topological nodes, and then normalized. The output from the grid registration is used to establish features correspondences between successive frames (Fig. 7(d)). Typical output from the optimization objective function produces a solution with an unambiguous minimum (Fig. 6).

## 5. Deformable grid registration

### 5.1. Topological mapping

Since the topology of the sheet metal surface is invariant under typical forming processes, planar topological maps were used to efficiently model the sheet metal surface features before and after deformation of the workpiece. This topological map representation is primarily used to reduce computational complexity. Although the workpiece has a three-dimensional shape, the location of each node in the (planar) map is specified using only two discrete degrees of freedom. The reduced dimensionality of this approach simplifies the computational effort required to construct, store, and match the topological maps.

Using the inter-frame grid tracking technique discussed in the previous section, new nodes are recorded with each new frame, and a global topological map of the entire sheet metal surface is built incrementally. A sample

global topological map (Fig. 8) was created from a video sequence containing 217 frames of a formed aluminum dome. The video was captured at 1.5 frames per second and is 2 minutes and 25 seconds in duration.

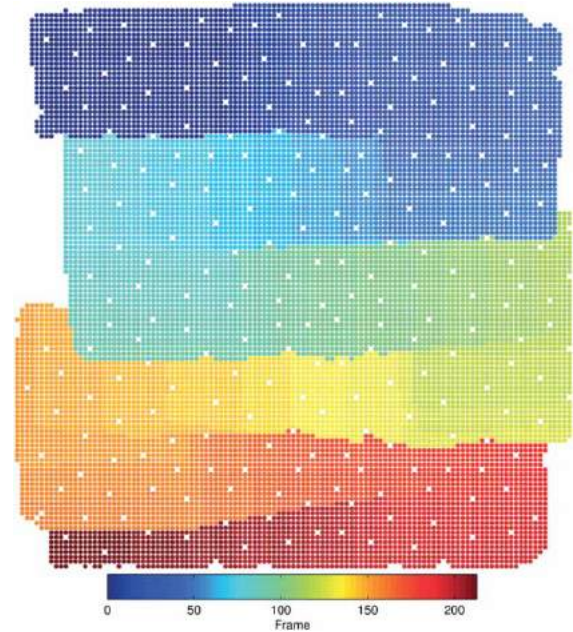


**Figure 8.** A global topological map of the sheet metal surface features. The color of each node is used to indicate the frame from which the dot-feature was first detected. Note the sweeping motion of the camera is easily discerned.

### 5.2. Map-model registration

To determine the correspondence between the imaged grid features (after deformation) and a model of the (unformed) grid geometry, the corresponding topological map representations are discretely shifted across one another. Then, an optimization objective function generates a scalar output for each tested grid shift. Once every feasible grid shift has been evaluated, the minimum value generated using the objective function determines the best estimate for true registration. The optimization objective function is defined as:

$$F(i, j) = \sum_{\substack{(u,v)|(u,v) \in M \\ (u+i,v+j) \in G}} (\sigma_{u,v}^M - \sigma_{u+i,v+j}^G)^2 + P(i, j) \quad (5.1)$$

where  $i, j$  define the grid shift and variables  $u, v$  denote the location of the node in each topological map.  $G$  designates the interior (subset) of the global map and  $M$  signifies the map of the (unformed) model geometry.  $\sigma$  denotes the fiducial metric associated with each node, and the penalty term  $P(i, j) = \sqrt{i^2 + j^2}$  represents the Euclidean distance of the grid shift.



Once the topological map of the deformed surface features has been matched with the model geometry, nodes are correlated between the corresponding topological map representations. The disparity between the formed geometry and the model coordinates can then be used to measure the expansion or compression of the grid pattern, and by extension, the principal surface strain values. Herein, we report novel algorithms and techniques to enable detection, tracking and registration of deformable gridded surfaces; an accuracy analysis of the final 3D reconstruction is beyond the scope of this paper.


## 6. Conclusion

An evaluation of several prominent image-based feature detectors demonstrated that the SURF algorithm was the most accurate and robust. SURF features were detected from an inkjet-printed dot-grid pattern with excellent detection coverage and fractional pixel error. A novel algorithm for close-range inter-frame motion tracking used negative fiducials and an optimization objective function to achieve robust grid registration. Planar topological maps of the sheet metal surface features were used to reduce dimensionality and simplify computation. Applications include visual measurement of surface strain for plastic vacuum or sheet metal press forming.

## Acknowledgements

Financial support for this work was received from the Natural Sciences and Engineering Research Council of Canada (NSERC) Discovery Grant program. Inkjet printing was performed at Mohawk College (Hamilton, ON, Canada). The sheet metal was provided by Dr. Mukesh Jain (McMaster University) and forming services were provided by Mike Bruhis (McMaster University). This paper is an extension of research reported in [12], and an earlier extended abstract of this paper was presented at CAD'15, London, UK, June 22–25, 2015 and is published as <http://dx.doi.org/10.14733/cadconfP.2015.402-407>.

## ORCID

Tyler S. Kenyon  <http://orcid.org/0000-0001-6604-7803>  
Allan D. Spence  <http://orcid.org/0000-0002-6835-6498>  
David W. Capson  <http://orcid.org/0000-0001-6981-780X>

## References

- [1] Autodesk Inc. AutoCAD®. San Rafael, CA.
- [2] Ayers, R. A.; Brewer, E. G.; Holland, S. W.: Grid Circle Analyzer - Computer Aided Measurement of Deformation, SAE Technical Paper 790741, 1979. <http://dx.doi.org/10.4271/790741>
- [3] Bay, H.; Ess, A.; Tuytelaars, T.; Van Gool, L.: Speeded-Up Robust Features (SURF), *Computer Vision and Image Understanding*, 110(3), 2008, 346–359. <http://doi.org/10.1016/j.cviu.2007.09.014>
- [4] Chan, H.-L.; Spence, A. D.; Sklad, M. P.: Laser digitizer-based sheet metal strain and surface analysis, *International Journal of Machine Tools and Manufacture*, 47(1), 2007, 191–203. <http://doi.org/10.1016/j.ijmachtools.2005.12.013>
- [5] Forming Technologies Inc.: *FormingSuite® Professional*. Burlington, ON. [www.forming.com](http://www.forming.com).
- [6] Garcia, D.; Orteu, J.: 3D Deformation measurement using stereo-correlation applied to experimental mechanics, *Proceedings of the 10th FIG International Symposium on Deformation Measurements*, 2001, 50–60.
- [7] Ghosh, A.: Effect of lateral drawing-in on stretch formability, *Metals Engineering Quarterly*, 15(3), 1975, 53–61.
- [8] GOM Argus. <http://www.gom.com>, GOM mbH.
- [9] Harris, C.; Stephens, M.: A Combined Corner and Edge Detector, *Proceedings of the Alvey Vision Conference*, 1988, 147–151. <http://dx.doi.org/10.5244/c.2.23>
- [10] Hecker, S. S.: A Simple Technique for Determining Forming Limit Curve, *Sheet Metal Industries*, 52(11), 1975, 671–676.
- [11] Intel Xeon Phi, <http://www.intel.com>, Intel Corporation.
- [12] Kenyon, T. S.: Close-Range Machine Vision for Strain Analysis, M.A.Sc. Thesis, McMaster University, 2014. <http://hdl.handle.net/11375/16324>
- [13] Kinsner, M.; Capson, D.; Spence, A.: Accurate measurement of surface grid intersections from close-range video sequences, *IEEE Transactions on Instrumentation and Measurement*, 61(4), 2012, 1019–1028. <http://doi.org/10.1109/TIM.2011.2174102>
- [14] Kinsner, M. H.; Kenyon, T. S.; Capson, D. W.; Spence, A. D.: Multiple View Motion Tracking of Gridded Surfaces using Topological Structure, *Computer-Aided Design and Applications*, 10(2), 2013, 221–229. <http://doi.org/10.3722/cadaps.2013.221-229>
- [15] Lindeberg, T.: Feature Detection with Automatic Scale Selection, *International Journal of Computer Vision*, 30(2), 1988, 79–116. <http://doi.org/10.1023/A:1008045108935>
- [16] Lowe, D. G.: Object recognition from local scale-invariant features, *Proceedings of the International Conference on Computer Vision*, 1999, 1150–1157. <http://doi.org/10.1109/ICCV.1999.790410>
- [17] Lowe, D. G.: Distinctive image features from scale-invariant keypoints, *International Journal of Computer Vision*, 60(2), 2004, 91–110. <http://doi.org/10.1023/B:VISI.0000029664.99615.94>
- [18] Matas, J.; Chum, O.; Urban, M.; Pajdla, T.: Robust wide-baseline stereo from maximally stable extremal regions, *Image and Vision Computing*, 22(10), 2004, 761–767. <http://doi.org/10.1016/j.imavis.2004.02.006>
- [19] Neubeck, A.; Van Gool, L.: Efficient Non-Maximum Suppression. *Proceedings of the 18th International Conference on Pattern Recognition*, 3(c), 2006, 850–855. <http://doi.org/10.1109/ICPR.2006.479>
- [20] NVIDIA CUDA-enabled GPU Hardware, <http://www.nvidia.com>, NVIDIA Corp.
- [21] POV-RAY, <http://www.povray.org>, Persistence of Vision Raytracer Pty. Ltd.
- [22] Roland DGA <https://www.rolanddga.com/>
- [23] Sowerby, R.; Duncan, J. L.; Chu, E.: The modelling of sheet metal stampings, *International Journal of Mechanical Sciences*, 28(7), 1986, 415–430. [http://dx.doi.org/10.1016/0020-7403\(86\)90062-7](http://dx.doi.org/10.1016/0020-7403(86)90062-7)

- [24] Tong, W.: Plastic Surface Strain Mapping of Bent Sheets by Image Correlation, *Experimental Mechanics*, 44(5), 2004, 502–511. <http://dx.doi.org/10.1007/BF02427962>
- [25] ViALUX AutoGrid, <http://www.vialux.de>, ViALUX Messtechnik + Bildverarbeitung GmbH.
- [26] Viola, P.; Jones, M. J.: Robust Real-Time Face Detection. *International Journal of Computer Vision*, 57(2), 2004, 137–154. <http://dx.doi.org/10.1023/B:VISI.0000013087.49260.fb>